applied sciences

MDPI

Article

Bionic Intelligent Algorithms Used in Helicopter Individual Blade Control Optimization

Yadong Gao [1], Dawei Huang [1,*], Xinyu Yu [1] and Huaqin Zhang [2]

[1] College of Aerospace Engineering, Nanjing University of Aeronautics and Astronautics, Nanjing 210001, China; gydae@nuaa.edu.cn (Y.G.); y1215225@nuaa.edu.cn (X.Y.)
[2] Commercial Aircraft Corporation of China Ltd. (COMAC), Shanghai 200126, China; zhanghuaqin@comac.cc
* Correspondence: damereywong@nuaa.edu.cn

Featured Application: Bionic intelligent algorithms demonstrate higher efficiency and accuracy compared with traditional control methods when solving the complex nonlinear system problems encountered in the research of dynamics. Bionic intelligent algorithms have great application prospects in the field of aeroelasticity dynamic control.

Abstract: Bionic algorithms are established by imitating human neural structures and animal social behaviors. As an important part of bionic technology, bionic algorithms are often used to solve the control problems of complex nonlinear systems, such as the rotor aeroelasticity dynamics model used in the helicopter individual blade control (IBC) optimization process. Two control methods based on bionic intelligent algorithms are introduced, respectively. The first method is to combine the fuzzy neural network and the classical PID control together. Compared with traditional PID control, the combined one was able to adjust the PID control parameters automatically by using the learning ability of the fuzzy neural network. The second method is to directly search the optimal control parameters by using the particle swarm algorithm. Both two methods demonstrate higher efficiency and accuracy; according to the results obtained by the algorithms, the vibration level was 80% less than without the applied high order harmonics. This indicates great application prospects for bionic intelligent algorithms in solving complex nonlinear system problems.

Keywords: bionic algorithm; artificial neural network (ANN); particle swarm algorithm (PSO); PID control; individual blade control (IBC); helicopter elastic aerodynamics

Citation: Gao, Y.; Huang, D.; Yu, X.; Zhang, H. Bionic Intelligent Algorithms Used in Helicopter Individual Blade Control Optimization. *Appl. Sci.* **2022**, *12*, 4392. https://doi.org/10.3390/app12094392

Academic Editors: Aihong Ji, Chengchun Zhang, Gang Chen and Zirong Luo

Received: 5 April 2022
Accepted: 24 April 2022
Published: 27 April 2022

1. Introduction

Helicopter individual blade control (IBC) aims to reduce vibration on the rotor and improve flight performance [1]. Due to the huge cost of the experiment, researchers always used theory model to calculate the load on the rotor. The rotor aeroelasticity dynamic model used in the process is a complex nonlinear multivariable system without explicit transfer functions. Traditional control methods (such as classical PID control) are no longer suitable in such situations. This paper designed two new control methods combined with bionic intelligent algorithms. As an important application of bionic technology in computer science, the bionic intelligent algorithms are developed by imitating the social behavior of animals and the structure of the human neuron. Compared with traditional control methods, bionic intelligent algorithms have advantages in solving nonlinear, multivariable and chaotic problems.

Presently, we outline a brief history of IBC technology experiments. Since December 2001, the ZFL company had carried out IBC flight tests using the CH-53G test bench at the Aircraft Engineering Center of the German Federal Defense Office; the IBC system used was designed and certified by ZFL [2]. The tests had demonstrated that without the explicit optimization of amplitude or phase, the IBC could reduce vibration by more

than 90% in a single direction, or in some cases by more than 60% in all directions. In the best-case scenario encountered during open-loop testing, an IBC of 2/rev was able to reduce variable-pitch tie-rod loads by more than 30%.

In 2002, Stephen A. Jacklin et al. conducted a full-scale UH-60A monolithic blade control study in the 80 ft × 120 ft wind tunnel at the NASA Ames Research Center to reduce flight noise and vibration [3]. The preliminary wind tunnel data obtained demonstrated that using a 3/rev harmonic of approximately 1.0° amplitude could reduce overall vibration by 70%, and using a 2/rev harmonic of 3.0° amplitude could reduce BVI noise by up to 12 dB (75%).

Tests with real rotors are too costly; therefore, the research uses surrogate models to calculate the load on the rotor after acting on the harmonic. The surrogate model of the rotor, called the aeroelasticity dynamic model, is just like a black box without explicit transfer functions. The inputs of the black box are the harmonic acting on the blade, and the output of the black box is the load on the rotor. The aim of the optimization is to find the most suitable input parameters of the system (harmonic phase and amplitude) to obtain the minimal output; thus, the process of optimization can be regarded as a process of control.

The artificial neural network (ANN) and particle swarm optimization (PSA) are used widely in solving black box problems. For example, Luong et al. proposed a neural network controller with supervised learning to simulate the behavior of a proven controller only with system states [4]. Jakubowski et al. presented unsupervised learning using a variational autoencoder to monitor the wear of rolls in a hot strip mill, which is a part of a steel-making site [5]. Kierzkowski et al. developed a simulation model to perform a sensitivity analysis of the energy consumption of an airport baggage handling system to change the resource allocation strategy [6].

However, there is not much application of bionic intelligent algorithms in the research of the aeroelasticity dynamic model. In this paper, two methods combined with the fuzzy neural network and particle swarm algorithm are presented, respectively.

The first method is to combine the fuzzy neural network and the classical PID control together. Compared with the traditional PID control, the combined one can adjust the PID control parameters automatically by using the learning ability of the fuzzy neural network. The second method is to search the optimal control parameters directly by using the particle swarm algorithm.

In this article, the bionic intelligent algorithms were used to search the best input parameters of the complex nonlinear system. This also provides a theoretical basis for the application of helicopter individual blade control technology in engineering. The results prove that bionic intelligent algorithms demonstrate higher efficiency and accuracy compared with traditional control methods, which indicates the great application prospect of such algorithms in solving complex nonlinear problems.

In Section 2.1, the aeroelasticity dynamic model of the helicopter rotor is briefly introduced. In Sections 2.2 and 2.3, two optimization algorithms are presented, respectively. In Section 3, the results of the optimization process are described. Section 4 contains conclusions of this work.

2. Methods

The optimization process can be regarded as an automatic process represented in Figure 1. The input of the system is high-order harmonics (including both amplitude and phase), and the output of the system is the load component of the rotor hub (the 3/rev component, used to reflect the vibration level of the whole rotor). The intermediate parts of the system are the bionic intelligent algorithm and rotor aeroelasticity dynamic model. (The algorithm is used to adjust the input, and the aeroelasticity dynamic model is used to calculate the load on the rotor hub). The purpose of the method is to get the minimal output value by adjusting the inputs.

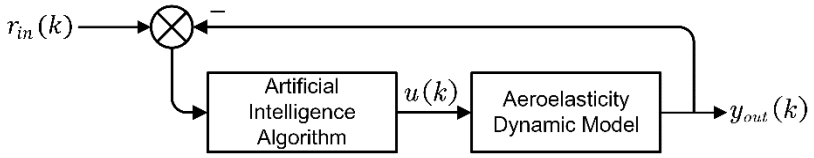

Figure 1. Schematic diagram of the control problem.

The focus of this article are the establishments of two bionic intelligent control algorithms and the rotor aeroelasticity dynamic model. The comparison of two methods are shown in Figure 2.

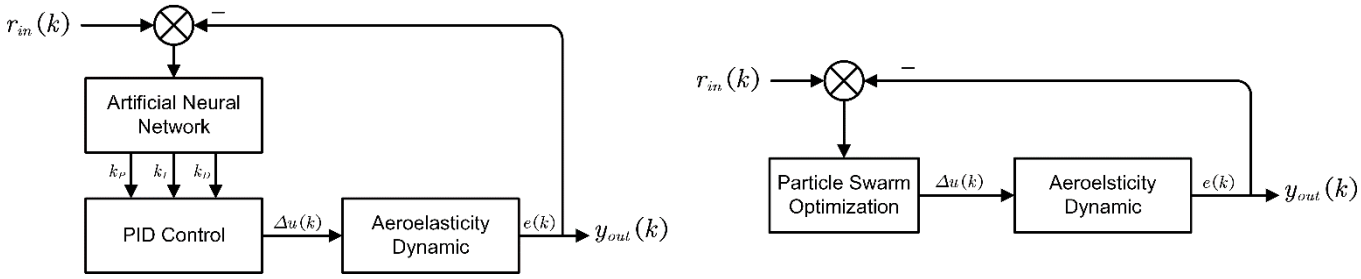

Figure 2. Comparison of two control methods. (**a**) Fuzzy neural network combined with PID control; (**b**) particle swarm optimization.

2.1. The Establishment of Rotor Aeroelasticity Model

The IBC technology controls every blade individually. As shown in Figure 3, high-order harmonics are acted onto each blade individually by the actuator.

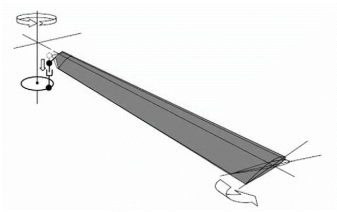

Figure 3. Helicopter individual blade control (IBC).

When studying the IBC technology, the rotor aeroelasticity dynamic model is always used to calculate the load on the rotor hub. The model consists of a dynamic model and an aerodynamic model. The former one is based on Hamilton's law of variation principle and Hodges neutral beam principle; the latter one is based on Leishman-Beddoes dynamic stall theory and the Pit-Pitters inflow theory model.

The helicopter rotor could be regarded as a conservative system. According to the Hamilton's law of variation principle [7], the total potential energy of the conservative system took the minimum value of the time integral from the start time to the end time. The energy expression of the equation was:

$$\delta\Pi = \int_{t_1}^{t_2} (\delta U - \delta T - \delta W)dt = 0 \quad (1)$$

Within the equation, δU was the variation of strain energy, δT was the variation of kinetic energy, and δW was the variation of external force virtual work.

By the discretization of time and space, the energy expression of the number b blade was:

$$\delta\Pi_b = \int_{t_2}^{t_2}\left[\sum_{i=1}^{N} r\Delta_i\right]dt = \int_{t_1}^{t_2}\left[\sum_{i=1}^{N}(\delta U_i - \delta T_i - \delta W_i)\right]dt \quad (2)$$

The key point was the calculation of the three parts. In formula above, δU_i and δT_i were calculated by the dynamic theory, and δW_i was calculated by aerodynamic theory.

2.1.1. Variation of Strain Energy δU_i

Assuming the blade was a slender isotropic beam, and $\sigma_{yy} = \sigma_{yz} = \sigma_{zz}$, the corresponding relationship could be described:

$$\sigma_{xx} = E\varepsilon_{xx} \;\; \sigma_{x\eta} = G\varepsilon_{x\eta} \;\; \sigma_{x\zeta} = G\varepsilon_{x\zeta} \quad (3)$$

where E was the blade elastic modulus, G was the blade shear modulus, σ_{xx} was the axial strain, and $\sigma_{x\eta}$ and $\sigma_{x\eta}$ were the blade shears' strain.

According to the above assumptions, the strain energy expression of the blade could be deduced as:

$$\delta U_b = \frac{1}{2}\iiint_0^R \left(\sigma_{xx}\delta\varepsilon_{xx} + \sigma_{x\eta}\delta\varepsilon_{x\eta} + \sigma_{x\zeta}\delta\varepsilon_{x\zeta}\right)d\eta d\zeta dx \quad (4)$$

According to the medium deformation theory, the pitch angle ε_{xx} and strain displacement $\varepsilon_{x\eta}$ $\varepsilon_{x\zeta}$ expressions of the blade could be expressed as:

$$\begin{cases} \varepsilon_{xx} = f_1\left(\phi\prime, \hat{\phi}\right) \\ \varepsilon_{x\eta} = f_2(\phi\prime) \\ \varepsilon_{x\zeta} = f_3(\phi\prime) \end{cases} \quad (5)$$

Bringing f_1, f_2, f_3 in the displacement expression, in the form of generalized force, it could be expressed as [8]:

$$\delta U_i = \delta q_i^T \cdot Q_i^E \quad (6)$$

2.1.2. Variation of Blade Kinetic Energy δT_i

The kinetic energy of the blade was mainly related to the blade speed. The speed consisted of two parts, one was the speed of the blade relative to the hub $\vec{V}_b$, and another was the speed of the hub itself, $\vec{V}_f$. The isolated rotor was considered in this article; thus, $\vec{V} = \vec{V}_b + \vec{V}_f$, and the velocity expression of any point on the blade in the hub coordinate system could be presented as:

$$\vec{V}_b = V_{bx}i + V_{by}j + V_{bz}k \quad (7)$$

Every item in the equation could be presented as the following:

$$\begin{cases} V_{bx} = \dot{x}_1 - \Omega y_1 cos\beta_p \\ V_{by} = \dot{y}_1 - \Omega x_1 cos\beta_p - \Omega z_1 sin\beta_p \\ V_{bz} = \dot{z}_1 - \Omega y_1 sin\beta_p \end{cases} \quad (8)$$

According to the relationship between strain and stress, the kinetic energy variational expression of the number b blade was:

$$\delta T_b = \iiint_0^R \left(\rho_s \vec{V}_b \cdot \delta\vec{V}_b\right)d\eta d\zeta dx \quad (9)$$

Finally, in the form of generalized force, it could be expressed as:

$$\delta T_i = \delta q_i^T \cdot Q_i^T \tag{10}$$

2.1.3. Variation of Virtual Work δW_i

To obtain the accurate rotor aerodynamic force, it was not only necessary to obtain an accurate induced velocity distribution on the rotor-disc, but also to establish an accurate airfoil aerodynamic model [9]. To calculate the induced velocity, the Pitt–Peters dynamic inflow model was used in this article. The induced velocity could be described along the azimuth of the paddle $\overline{\psi}$ and the blade span $\overline{r}$:

$$\overline{v}_i(\overline{r}, \overline{\varphi}) = \lambda_0 + \lambda_{1c}\frac{r}{R}cos\psi + \lambda_{1s}\frac{r}{R}sin\psi \tag{11}$$

The Leishman–Beddoes unsteady dynamic stall aerodynamic model was used to calculate the aerodynamic force. This model described the relationship between the lift and the angle of attack.

The Figure 4 showed the force and moment acting on the profile. The lift moment L, drag moment C, and aerodynamic moment M on the profile could be expressed combined with the forward flight speed V:

$$\begin{cases} L = \frac{1}{2}\rho V^2 c C_N \\ C = \frac{1}{2}\rho V^2 c C_C \\ M = \frac{1}{2}\rho V^2 c C_C \end{cases} \tag{12}$$

This model described the relationship between the lift and the angle of attack. The normal force coefficient C_N, chord force coefficient C_C, and pitch moment coefficient C_M needed to be calculated.

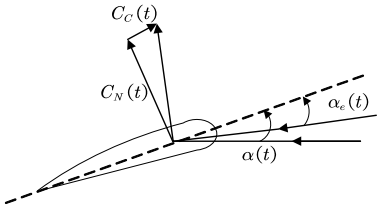

Figure 4. Actual angle of attack (AOA).

- **Normal force coefficient** C_N;

When the airfoil angle of attack changes $\Delta\alpha$, the circulation normal force response could be expressed as:

$$(C_N)_n = \left(C_N^C\right)_n + \left(C_N^I\right)_n + \left(C_N^q\right)_n \tag{13}$$

$$\begin{cases} \left(C_N^C\right)_n = C_{L\alpha}(M)(\alpha_n - X_n - Y_n) \\ \left(C_N^I\right)n = \frac{4k_I T_I}{M}\left(\frac{\Delta\alpha_n}{\Delta t} - D_n\right) \\ \left(C_N^q\right)n = \frac{-k_I T_I}{M}\left(\frac{\Delta q_n}{\Delta t} - D_n^q\right) \end{cases} \tag{14}$$

- **Chord force coefficient** C_C;

$$(C_C)_n = (C_N)_n tan\alpha_e \tag{15}$$

- **Pitching moment coefficient** C_M;

$$(C_M)_n = \left(C_M^C\right)_n + \left(C_M^I\right)_n + \left(C_M^q\right)_n \tag{16}$$

$$\begin{cases} \left(C_M^C\right)_n = \left(\frac{1}{4} - x_{ac}\right)\left(C_N^C\right)_n \\ \left(C_M^I\right)n = -\frac{1}{4}\left(C_N^I\right)_n \\ \left(C_M^q\right)n = -\frac{1}{4}\left(C_N^q\right)_n - \frac{k_I^2 T_I}{3M}\left(\frac{\Delta q_n}{\Delta t} - D_n^{q\prime}\right) \end{cases} \tag{17}$$

According to the above equations, the corresponding external force virtual work coefficient (blade aerodynamic force) could be calculated.

The generalized expression for the final aerodynamic virtual work (blade aerodynamic force) could be written as:

$$\delta W_i = \delta q_i^T \cdot Q_i^A \tag{18}$$

2.1.4. Summarize

The three terms in the equation could be obtained according to the above equations to established the aeroelasticity dynamic model of the rotor.

$$\delta \Pi_b = \int_{t_1}^{t_2} (\delta U_i - \delta T_i - \delta W_i) dt = 0 \tag{19}$$

The model was a complex nonlinear system without explicit transfer functions, which was difficult to deal with traditional optimization methods.

To solve the problem, two methods combined with artificial intelligent algorithms were presented in the following article.

2.2. Fuzzy Neural Network Combined with PID Controller

Conventional PID control needs the specific transfer function of the controlled object, but the rotor aeroelasticity dynamic model had no explicit transfer function. Section 2.2 establishes a method that combines the fuzzy neural network and classical PID control together; the learning ability of fuzzy neural network was used to adjust the parameters of the PID control automatically.

The diagram of the classical PID control system is as Figure 5:

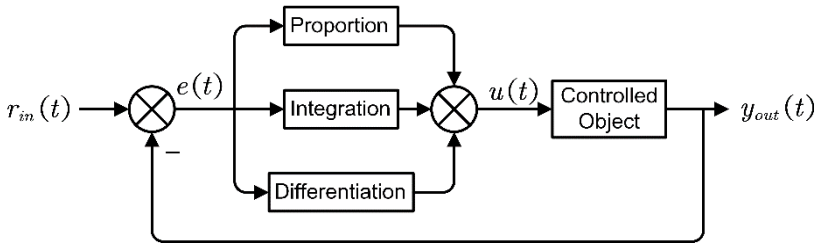

Figure 5. Schematic diagram of conventional PID control system.

The classical PID method controlled the controlled object according to the error between the actual output value of the controlled object and the reference value. The parameters (K_p, T_i, T_d) were stable. The relationship between the error $e(t)$ and $u(t)$ was as follows:

$$u(t) = K_p\left[e(t) + \frac{1}{T_i}\int_0^t e(t)dt + T_d\frac{de(t)}{dt}\right] \tag{20}$$

For the helicopter aeroelasticity dynamic model, the three parameters of the PID controller (proportional coefficient K_p, integral time constant T_i, and differential time constant T_d) were difficult to determine. Fuzzy neural network was introduced to adjust the parameters automatically.

The fuzzy neural network combined the characteristics of fuzzy control and the artificial neural network in a structurally equivalent way, and realized the design of the fuzzy controller through the training and learning of the neural network.

2.2.1. Fuzzy Control

Fuzzy controlled method solves complex nonlinear systems by some qualitative and uncertain control rules. Figure 6 shows the structure of a typical fuzzy controller.

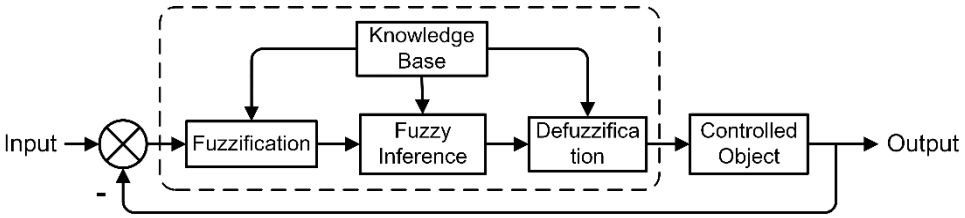

Figure 6. Fuzzy controller system structural.

The fuzzy controller was mainly composed of four parts: fuzzification, fuzzy inference, defuzzification, and knowledge base. Fuzzification was to convert input quantities with clear values into fuzzy vectors; fuzzy inference was to classify fuzzy vectors according to multiple rules formulated by fuzzy concepts; defuzzification was to process the output quantities obtained through fuzzy inference to obtain a clarity amount that can be used for actual control. The knowledge base was a collection of data and fuzzy rules.

2.2.2. Artificial Neural Network (ANN)

Artificial Neural Network (ANN) was established by imitating the structure of the human neuron system, which had a high adaptive ability and learning ability [10]. Figure 7 showed the structure of the human neuron.

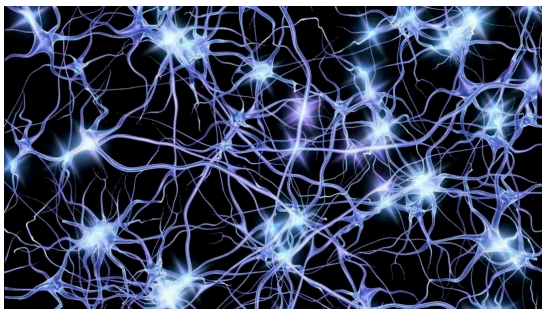

Figure 7. Human neuron.

A typical BP neural network was composed of an input layer, a hidden layer, and an output layer. The signals transmitted forward and the errors transmitted reversely. When the result was inconsistent with the reference result, the error was propagated back, and the connection weights and thresholds of the neural network were adjusted according to the learning algorithm until the reference value is reached.

The structure of the neural network is as in Figure 8:

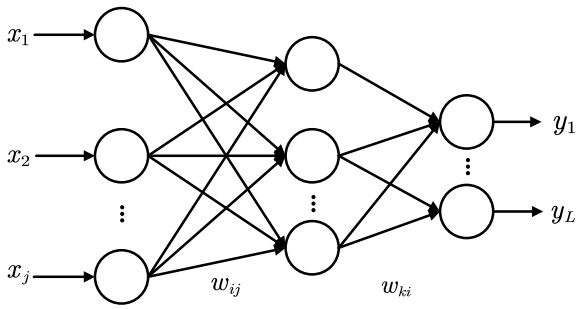

Figure 8. Topological structure of a typical BP neural network.

BP neural network consisted of input variables $X = (x_1, x_2, \ldots, x_m)$, hidden layers q, and output nodes $Y = (y_1, y_2, \ldots, y_m)$.

The input calculation equation of the node i in the hidden layer is as follows:

$$net_i^p = \sum_{j=1}^{M} \omega_{ij} o_j^p - \theta_i = \sum_{j=1}^{M} \omega_{ij} x_j^p \quad (i = 1, 2, \cdots, q) \tag{21}$$

In the above equations, x_j^p and o_j^p, respectively, represented the input and output of the input layer node under the action of the sample p, ω_{ij} represented the connection weight between the input layer node and the hidden layer node, and θ_i represented the threshold of the hidden layer node.

If the error of output exceeds the set value, the error was fed back from the output layer, and the connection weights between the neuron nodes of each layer were modified until the error was less than the set value. The quadratic error for the output of any sample was expressed as:

$$J_p = \frac{1}{2} \sum_{k=1}^{L} \left(t_k^p - o_k^p \right)^2 \tag{22}$$

The total error expression of the system was:

$$J = \sum_{p=1}^{N} J_p = \frac{1}{2} \sum_{p=1}^{N} \sum_{k=1}^{L} \left(t_k^p - o_k^p \right)^2 \tag{23}$$

The main function of the ANN was the weight correction between the three layers.

- Correction of the connection weight between the output layer and the hidden layer

The connection weights between the neuron nodes of each layer were adjusted in the opposite direction of the gradient of the error function.

The adjustment expression of the connection weight $\Delta\omega_{ki}$ could be obtained as:

$$\Delta\omega_{ij} = \eta \delta_k^p o_i^p = \eta_k^p \left(1 - o_k^p \right) \left(t_k^p - o_k^p \right)_i^p \tag{24}$$

Among the equation, t_k^p and o_i^p represented the expected result and the output value of the hidden layer node, respectively.

- Correction of the connection weights between the input layer and the hidden layer

In the same way, the modified expression of the connection weight between the hidden layer and the input layer could be obtained by the gradient of the error function:

$$\Delta\omega_{ij} = \eta \delta_i^p o_i^p = \eta o_i^p \left(1 - o_i^p \right) \left(\sum_{k=1}^{L} \delta_k^p \cdot \omega_{ki} \right) o_j^p \tag{25}$$

Among the equation, o_i^p and o_j^p, respectively, represented the output of the hidden layer neuron node i and the output of the output layer neuron node j under the action of the sample p.

Therefore, the weighting coefficient increment of the output layer node k and the connection weight increment of the hidden layer node i could be obtained under the action of the sample p:

$$\begin{cases} \omega_{ki}(k+1) = \omega_{ki}(k) + \eta \delta_k^p o_i^p \\ \omega_{ij}(k+1) = \omega_{ij}(k) + \eta \delta_i^p o_j^p \end{cases} \tag{26}$$

The connection weights of each layer of the neural network were adjusted to appropriate values, until the error is no more than the set value.

2.2.3. Fuzzy Neural Network

A new method was established by combining the characteristics of fuzzy control and the artificial neural network together. The learning ability of the neural network was introduced into the fuzzy system, and four parts of the fuzzy system were represented by the distributed neural network [11].

The Figure 9 showed the structure of the fuzzy neural network. The input layer passed the value of the input variable x_i to the next layer. The second layer, the fuzzification layer, received the values passed from the input layer and performs as fuzzification processing. Each node in this layer represented the value of a language variable and acted as a membership function to calculate the input variables. The membership degree was: $\mu_i^j (i = 1, 2, \ldots, n; j = 1, 2, \ldots, m)$, with the Gaussian function, as the membership function is as follows:

$$\mu_i^j = e^{-\frac{(x_i - c_{ij})^2}{\sigma_{ij}^2}} \tag{27}$$

Among the equation, c_{ij} represented the center of the Gaussian membership function, σ_{ij} represented the width of the Gaussian membership function, the connection weight of this layer was 1, and the number of nodes in this layer was $N_2 = \sum_{i=1}^{n} m_i$.

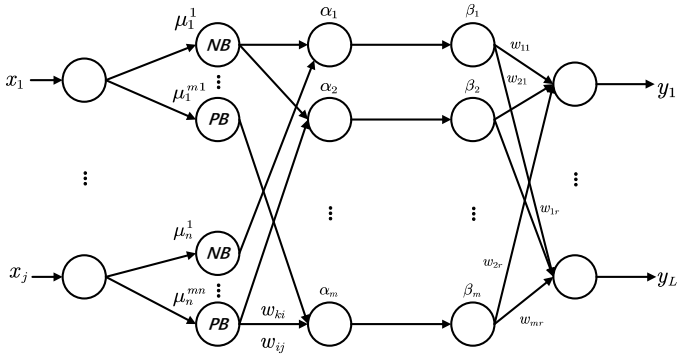

Figure 9. Diagram of Mamdani fuzzy neural network structure.

The third layer was the fuzzy inference layer, where each node corresponded to a fuzzy control rule. The neurons of the fuzzy inference layer corresponded to the antecedents of the fuzzy rules, and the applicability of each fuzzy rule was calculated in the form of a product. The expression is as follows:

$$\begin{gathered} \alpha_j = \mu_1^{i1} \mu_2^{i2} \cdots \mu_n^{in} \\ i_1, i_2, \cdots, i_n \in \{1, 2, \cdots, m\}; \quad j = 1, 2, \cdots, m; m = \prod_{m}^{n} m_i \end{gathered} \tag{28}$$

The connection weights of the fuzzy inference layer were all *1*. When the input to this layer was constant, only the linguistic variable values around the input had a larger membership function value, and the membership function values far away from the linguistic variable area are relatively large. If it was small, it would be treated as *0* during the calculation.

The function of the fourth layer was to convert a dimensional expression into a dimensionless expression in the inference process of the fuzzy neural network. The number of nodes in this layer was the same as that in the fuzzy inference layer. The expression is as follows:

$$\beta_j = \alpha_j / \sum_{j}^{m} \alpha_j \qquad j = 1, 2, \cdots, m \tag{29}$$

The fifth layer was the defuzzification layer with the function to convert the fuzzy amount into a precise amount; the expression is as follows:

$$y_i = \sum_{j=1}^{r} \omega_{ij} \beta_j \tag{30}$$

Among the equation, ω_{ij} represented the connection weight between the fourth layer and the fifth layer.

The fuzzy neural network combined the advantages of the language variable description of the fuzzy controller and the advantages of the self-learning ability of ANN in the structure of the fuzzy neural network. The center value c_{ij}, width value σ_{ij} of the Gaussian membership function, and the connection weight ω_{ij} could be adjusted automatically.

A fuzzy neural network was established. The following work is to combine the fuzzy neural network with the classical PID control together. The fuzzy neural network was used to adjust the PID control parameters automatically. Combined with the rotor aerodynamic model established in Section 2.1, the optimization process is shown in Figure 10:

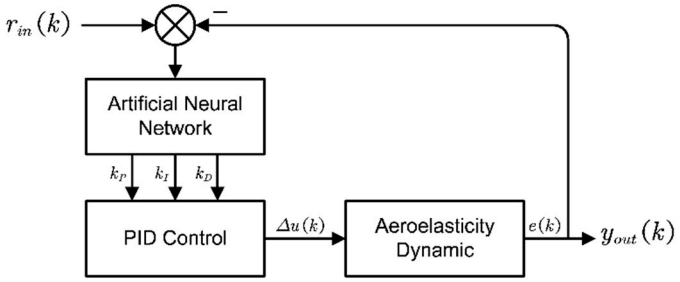

Figure 10. Fuzzy neural network PID control system structure.

In this system, the input $r_{in}(k)$ was the increment of the second-order harmonic cosine component, and the output $y_{out}(k)$ was the 3/rev component of the vertical force on the rotor hub. The expected value was the minimal vertical load of the rotor hub, which was set according to a specific requirement. In addition, the output of the fuzzy neural network PID control was the second-order harmonic cosine component, which is expressed as:

$$\Delta u(k) = k_p(e(k) - e(k-1)) + k_i \cdot e(k) + k_d(e(k) - 2e(k-1) + e(k-2)) \tag{31}$$

2.3. Swarm Optimization Algorithm

Particle swarm optimization imitated the social behaviors of animals or insects (bees, ants, et al.). The principle of particle swarm optimization was to imitate the ability of foraging food.

2.3.1. The Basic Theory of Particle Swarm Optimization

Figure 11 showed the bee colony that offered many inspires for scientist. The general process of the particle swarm optimization algorithm is to initialize a group of random particles, and finds the optimal solution by iteratively improving the fitness value of the function. In each iteration of the optimization function, the particle updated its velocity and position by pursuing two extremums: the individual extremum $(pbset_i)$ and the global extremum $(gbset_i)$.

Figure 11. Bee colony.

The total number of particles in the particle swarm was $popsize$, the dimension of the particle was m, and the stopping condition of the algorithm was the maximum number of iterations $maxiter$. The individual extremum and the group extremum were, respectively, $pbest_i(t) = [p_{i1}(t), p_{i2}(t), \ldots, p_{im}(t)]^T$ and $gbset = [g_1, g_2, \ldots, g_m]^T$, and all particles fly in the search space, according to the following updated form, to find the optimal solution:

$$v_{i+1}(t+1) = \omega v_i(t) + c_1 r_1(pbset_i(t) - x_i(t)) + c_2 r_2(gbset - x_i(t)) \quad (32)$$

$$x_{i+1}(t+1) = x_i(t) + v_{i+1}(t+1) \quad (33)$$

In the above equations, ω was the inertia weight coefficient, which determined how much the iteration speed was retained. c_1 and c_2 were the learning factor of the algorithm, and r_1 and r_2 were random numbers between $[0, 1]$.

2.3.2. The Basic Process of Particle Swarm Algorithm

1. Parameters such as population size, variable range, inertia weight, and learning factor were set, and a group of particles randomly initialized, which are uniformly distributed in a given optimization space.
2. The fitness value (function value) of each particle in the population was calculated. The fitness value of the number i particle was set to its current individual value $pbest_i$, and the optimal particle among all particles was set to the overall extremum of the population $gbest$.
3. For all particles, their current value was compared with the optimal value it has searched before. If the current position was better, the individual optimal position $pbest_i$ was set as the current position, and then the global value $gbest$ was updated.
4. The speed and position of each particle according to the equations was updated.
5. The given termination condition was determined whether it was satisfied. If it was met, the search was stopped and the required result was outputted; otherwise, Step 3 was returned to, in order to continue the optimization progress.

The process of a particle swarm algorithm is shown in Figure 12:

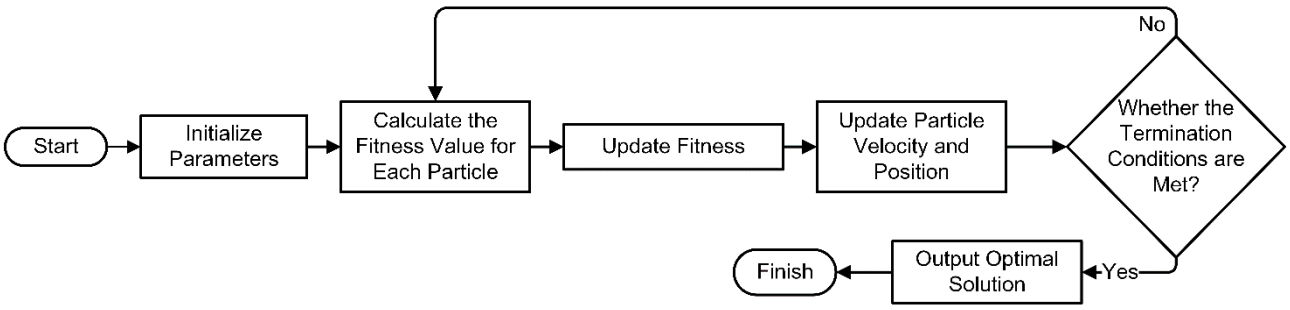

Figure 12. Flow chart of particle swarm algorithm.

2.3.3. Control Parameters of Particle Swarm Optimization

The velocity ω contained three parts: $\omega v_i(t)$, $c_1 r_1(pbest_i(t) - x_i(t))$ and $c_2 r_2(gbest - x_i(t))$. The inertia weight ω played a role in balancing the local search ability and the global search ability. According to experience, the range of inertia weight was $[0.9, 1.2]$.

A larger weight ω was helpful for global search, and a smaller one was helpful for local search. To achieve a balance between two aspects, the inertia weight ω was designed to decrease along with the increase in the calculation number. The decrease equation of inertia weight ω was as follows:

$$\omega = \omega_{max} - \frac{t}{t_{max}}(\omega_{max} - \omega_{min}) \tag{34}$$

Among the equation, ω_{max} was the maximum weight, ω_{min} was the minimum weight, and t_{max} was the maximum number of iterations. According to experience, the value was $\omega_{max} = 0.9, \omega_{min} = 0.4$.

Specifically, in this method, the amplitude and phase of the second-order harmonic were used as the parameter values of each particle, and the rotor load was used as the fitness to measure the fitness of each particle. The optimization system is shown in Figure 13:

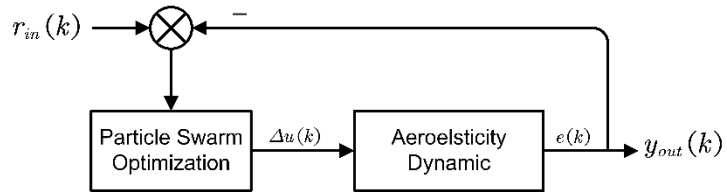

Figure 13. Control model of swarm algorithm.

The input of the system were the amplitude and phase of the second-order harmonic, and the output of the system was the 3/rev component of the vertical force on the rotor hub. The expected output value is the load on the rotor, which was set according to specific requirement.

The difference between the fuzzy neural network PID control and the swarm optimization was that the output of the latter process was the parameters of the second-order harmonic directly, and no other control parameters were adjusted.

Two methods were used to search the optimal input of the aeroelasticity dynamic model.

3. Results

The results include two sections, Section 3.1 illustrates the validation of the aeroelasticity dynamic model established in Section 2.1; Section 3.2 illustrates the results obtained by the optimization algorithm.

3.1. Validation of Aero-Elasticity Dynamic Model

This section is the validation of the aero-elasticity dynamic model; this article validated it from a different perspective. For example, the response of the tip flapping and lift coefficient represents the moment and force on the rotor, and the stability of the two parameters reflect the reliability of the aero-elasticity model.

In the hovering state, the aerodynamic environment of the rotor paddle was unsteady, so the response of the blade tip flapping and the response of the lift coefficient remained unstable. In this paper, the isolated rotor model was adopted, and the collective pitch in the hovering state was $\theta = 6°$. The dimensionless response of the blade tip flapping and lift coefficient in the hovering state were obtained by bringing in the aeroelasticity dynamic model, as shown in Figures 14 and 15:

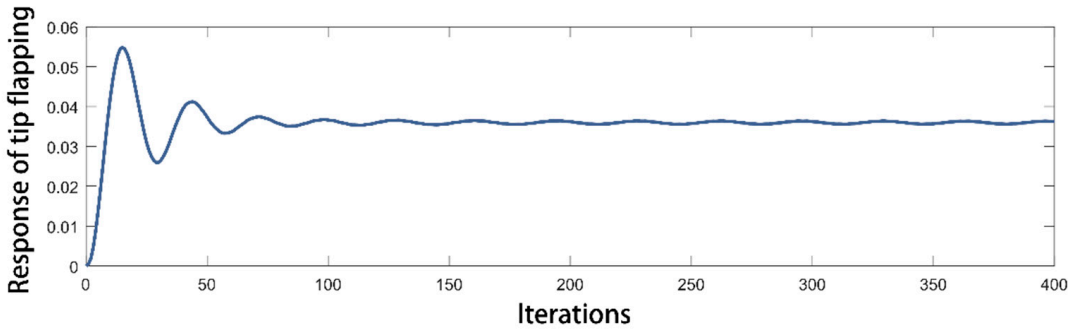

Figure 14. Response of blade tip flapping.

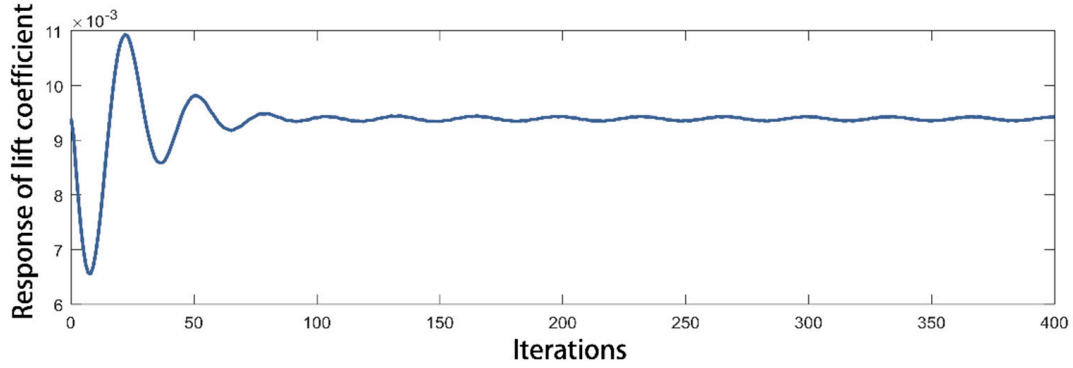

Figure 15. Response of rotor lift coefficient.

The calculation process of the model was an iterative flow. The response of tip flapping in Figure 14 reflects the bending moment of the blade, and the response of lift coefficient in Figure 15 reflects the overall lift of the whole rotor. If the two parameters convergence after several iterations, it means that the aeroelasticity dynamic model is feasible. This model has been modified several times and the sample data selected has been proven to be reliable; thus, both the response of tip flapping and lift coefficient converged quickly. Figures 14 and 15 show that when the number of iterations is reached about 150 times, the blade tip flapping response converges, while the blade lift coefficient converges when the number of iterations is reached about 120 times. The validation results proved that the aeroelasticity dynamic model had good stability.

Because of the uneven inflow and induced velocity distribution, the hub load was in a periodic change. Before the calculation of forward flight state, the collective pitch and periodic pitch in the steady state needed to be given. In this paper, the obtained state parameters are shown as follows:

The trim parameters calculated in Table 1, above, were substituted into the aeroelasticity dynamic model to obtain the hub vibration load. Among the three forces and three moments on the hub, the vertical force of the hub had the greatest influence on the vibration of the fuselage. The vertical force load of the hub under the forward flight state was obtained through the calculation in Figure 16:

Table 1. Parameters in forward flight.

Parameter	Value
Advanced ratio μ	0.3
Lift coefficient C_T	0.0072
Collective pitch $\theta_0/(^\circ)$	6
Horizontal periodic pitch $\theta_{1c}/(^\circ)$	2.75
Longitudinal periodic pitch $\theta_{1s}/(^\circ)$	−4.76

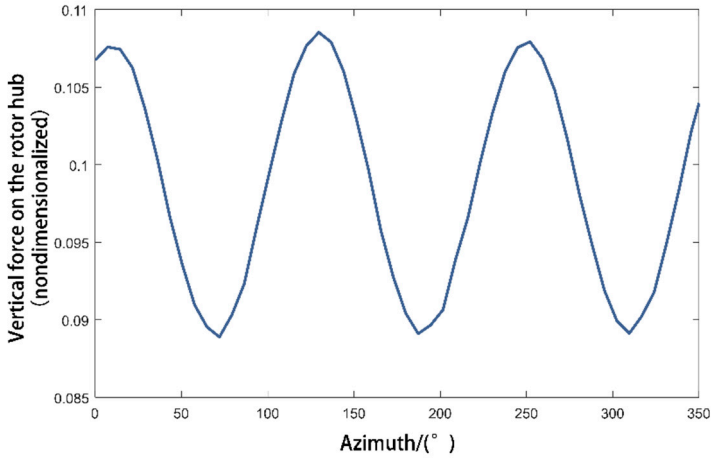

Figure 16. Vertical force on the rotor hub (nondimensionalized).

Because the model used in this article consisted of three blades, the period of the force in Figure 16 was nearly 120°; if there were N blades, the period would be 360°/N. This means that the rotor underwent three periods in 1/rev. However, due to the complex air flow environment and the difference between each blade, the force was not a strict harmonic wave. Figure 16 showed that there was some slight difference between each period. By extracting the response of the hub vertical force within a period by FFT, the harmonic component of the hub vertical force could be obtained:

The 0-order force in Figure 17 represented the average force on the rotor (the lift), as the higher order force represented the vibration load. As shown in Figure 17, for a rotor with three blades, the hub vertical force of 3/rev was an important part of the hub vertical load, and the 6/rev was too little to be considered To reduce the vibration load of the helicopter, the paper took a 3/rev harmonic load component as the controlled object to calculate and analyze.

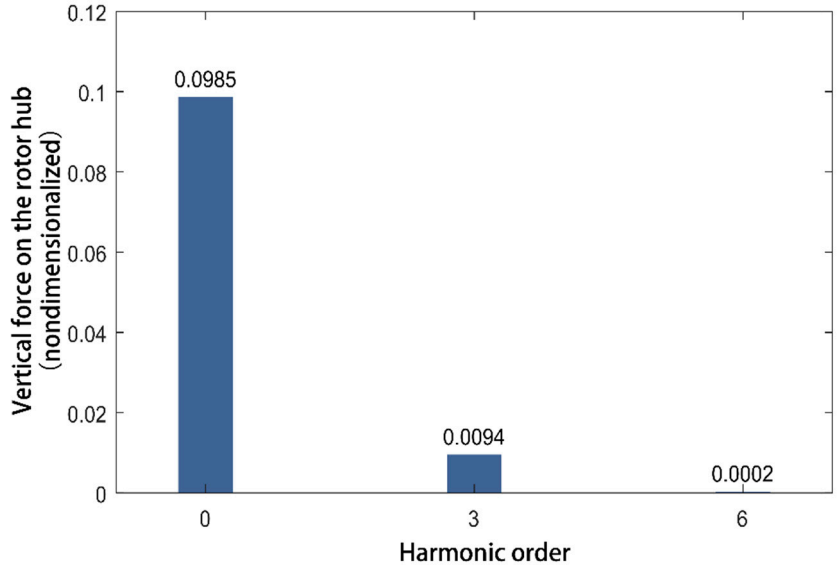

Figure 17. Vertical force on the rotor hub divided into harmonic components (nondimensionalized).

3.2. Results of Fuzzy Neural Network PID Method

The inputs of the system were the amplitude and phase of the second-order har-monic, and the output of the system was the 3/rev component of the vertical force on the rotor hub. The expected output value is the load on the rotor, which was set according to specific requirements. This article calculated the output by the dynamic model, and adjusted the

input according to the error between the output and expected output by the optimization. For a rotor with high-order harmonic control components, the pitch variation of the $b-th$ blade was expressed as [12]:

$$\begin{aligned}\left(\theta_{pitch}\right)_{IBCb} = \theta_0 + \theta_{1c}cos\left(\Omega t + (b-1)\tfrac{360^\circ}{N_b}\right) + \theta_{1s}sin\left(\Omega t + (b-1)\tfrac{360^\circ}{N_b}\right) \\ + \sum_{i=2}^{order} \theta_i cos\left[i\left(\Omega t + (b-1)\tfrac{360^\circ}{N_b}\right) + \phi_i\right]\end{aligned} \quad (35)$$

Both the magnitude and phase of the second harmonic influenced the hub load. In this article, the isolated rotor was considered and the influence of the second-order harmonics on the rotor hub load was calculated by the aeroelasticity dynamic model.

Taking the amplitude and phase of the harmonics as independent variables and the change of the hub load after loading the harmonics as the dependent variables, the variation of the load on the hub is shown in Figures 18 and 19 [13–15]:

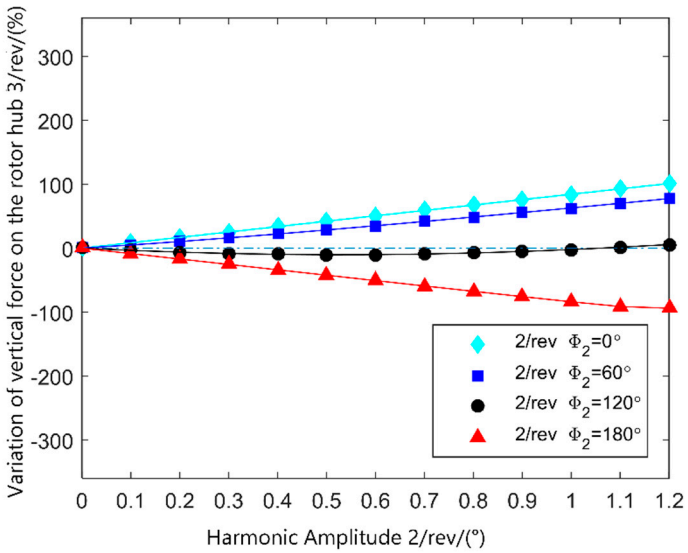

Figure 18. The variation of the average component of the vertical force on the rotor with the amplitude of the second-order harmonic.

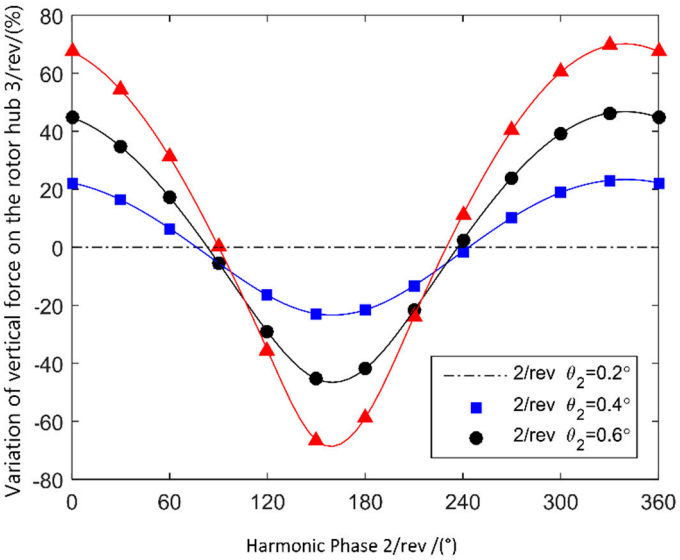

Figure 19. The variation of the average component of the vertical force on the rotor with the phase of the second-order harmonic.

Figures 18 and 19 reflect the influence of amplitude and phase on the hub load, respectively. The effects of harmonic amplitude and phase on the hub load are non-linear. When the value of the phase is at around 180°, a minimal force is achieved [16–19].

Therefore, the sine component of the second-order harmonic could be set to 0, the input of the system was the increment of the cosine component of the second-order harmonic Δu_k, and the output was the 3/rev component of the vertical force on the rotor $y_{out}(k)$. The expected output was set to be 20% of the initial vibration value. The process of optimization is shown in Figure 20:

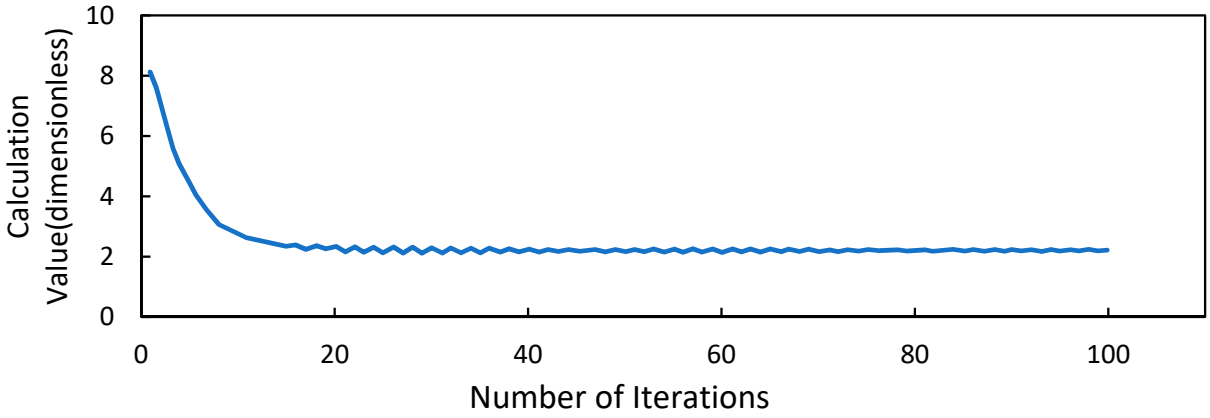

Figure 20. The process of optimization of fuzzy neural network PID control.

Figure 20 shows that the 3/rev vertical force on the rotor hub was in a reduced trend, and there was no obvious excitation in the whole process. When the 40th control calculation was finished, the vertical force reached the predetermined value. Figure 16 also shows that the fuzzy neural network PID method had a good effect on the optimization of a nonlinear complex system [20–23].

3.3. Results of Swarm Particle Optimization

Different from the fuzzy neural network method above, in the process of particle swarm algorithm, the amplitude and phase of the second-order harmonic were adjusted directly. The input of the system was the second-order harmonic Δu_k, and the output was the 3/rev component of the vertical force on the rotor $y_{out}(k)$. The expected output was set to be as minimal as possible [24].

The parameter settings used in the particle swarm algorithm are shown in the following Table 2:

Table 2. Particle swarm optimization parameters.

Parameter	Value
Inertia weight w	$w_{max} = 0.9, w_{min} = 0.4$
Learning factor c_1, c_2	$c_1 = c_2 = 2$
Particle population size Q	50
Domains of each dimensions	$[-3, 3]$
Iteration numbers n	100
Particle velocity V_{max}, V_{min}	$V_{max} = 2, V_{min} = -2$

The process of optimization is shown in Figure 21:

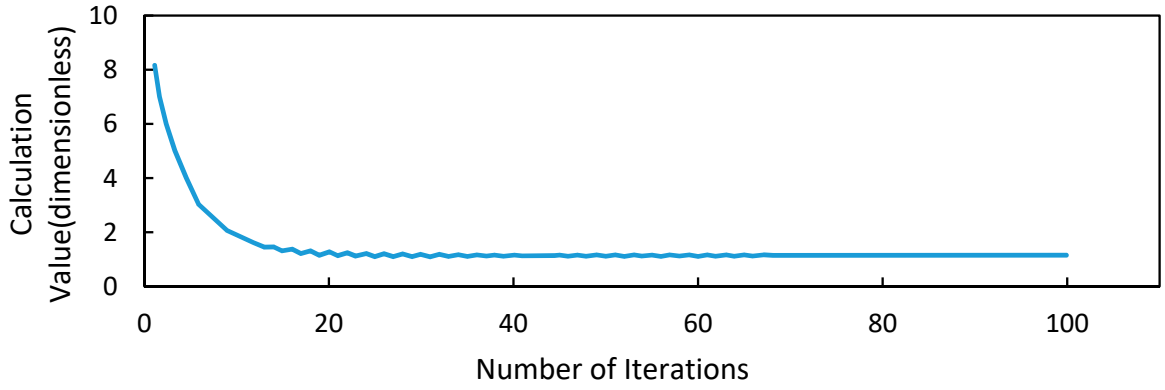

Figure 21. The variation trend of vertical force under particle swarm optimization method.

As shown in Figure 21, during the process of 100 iterations, the fitness function could converge quickly. After about 40 iterations, the fitness value converged.

Compared with the fuzzy neural network PID method, the particle swarm optimization could get a combination of harmonic parameters with a better vibration reduction effect [25–29]. The results also reflected that both two methods have a good effect on the optimization of this aeroelasticity dynamic model.

4. Conclusions

In this paper, two methods based on the bionic intelligent algorithms were established to be used in the optimization of helicopter individual blade control (IBC) [30]. The first method was the combination of the fuzzy neural network algorithm and traditional PID control, and the second one was the swarm particle optimization algorithm. The optimization of the complex nonlinear system could be regarded as a control problem that could not be handled by traditional methods easily.

In previous research, traditional control methods were used to deal with the complex dynamic problems, which always faced difficulties such as hard to determine control parameters and not converging quickly. This paper solved this problem by using some new algorithms, and ideal results were obtained [31]. According to the results obtained by the algorithms, the vibration level was 80% less than without the applied high-order harmonic.

The isolated rotor of the helicopter studied in this paper was in a stable forward flight state, but the helicopter often encounters unstable states such as the maneuvering flight and side-wind during the flight. How to research the problem in such situations is still worth exploring. At the same time, harmonics above the second order can also be applied in the actual control process [32,33]. When the number of control parameters increases, it is worth researching whether the method still works.

The paper also provides a theoretical basis for the application of helicopter IBC technology in engineering.

Author Contributions: Conceptualization, methodology, and software, D.H., H.Z. and X.Y.; writing—original draft preparation and writing—review and editing, D.H.; supervision and project administration, Y.G.; funding acquisition, Y.G. All authors have read and agreed to the published version of the manuscript.

Funding: This research is a project funded by the Priority Academic Program Development of Jiangsu Higher Education (PAPD).

Institutional Review Board Statement: Not applicable.

Informed Consent Statement: Not applicable.

Data Availability Statement: For those who are interested in our work, they can download our code in the following link: https://gitee.com/ainide28/applsci-1691450.git (accessed on 2 April 2022).

Conflicts of Interest: The authors declare no conflict of interest.

References

1. Wilbur, M.L.; Wilkie, W.K. Active-Twist Rotor Control Applications for UAVs. *Transform. Sci. Technol. Curr. Future Force* **2004**, *4*, 185–192.
2. Arnold, U.T.P. Recent IBC Flight Test Results from the CH-53G Helicopter. In Proceedings of the 29th European Rotorcraft Forum, Friedrichshafen, Germany, 1–18 September 2003; pp. 1–15.
3. Jacklin, S.A. Second Test of a Helicopter Individual Blade Control System in the NASA AMES 40 by 80 Foot Wind Tunnel. In Proceedings of the 2nd International American Helicopter Society Aeromechanics Specialists Conference, Bridgeport, CT, USA, 11 October 1995.
4. Luong, Q.V.; Jo, B.H.; Hwang, J.H.; Jang, D.S. A Supervised Neural Network Control for Magnetorheological Damper in an Aircraft Landing Gear. *Appl. Sci.* **2022**, *12*, 400. [CrossRef]
5. Jakubowski, J.; Stanisz, P.; Bobek, S.; Nalepa, G.J. Anomaly Detection in Asset Degradation Process Using Variational Autoencoder and Explanations. *Sensors* **2022**, *22*, 291. [CrossRef] [PubMed]
6. Kierzkowski, A.; Kisiel, T. Simulation Model for the Estimation of Energy Consumption of the Baggage Handling System in the Landside Area of the Airport. *Energies* **2022**, *15*, 256. [CrossRef]
7. Lanczos, C. *The Variational Principles of Mechanics*; University of Toronto Press: Toronto, ON, Cananda, 1949.
8. Peter, D.; John, D. Nonlinear Stall Flutter and Divergence Analysis of Cantilevered Graphite/Epoxy Wings. *AIAA J.* **2012**, *30*, 153–162.
9. Stepniewski, W. *Rotary-Wing Aerodynamics*; Dover Pub Inc.: Dover, Germany, 1984.
10. Zhu, D. Research Status and Prospect of Artificial Neural Network. *J. Jiangnan Univ.* **2004**, *3*, 106–113.
11. Ozyildirim, M.B. One Pass Learning for Generalized Classifier Neural Network. *Neural Netw. Off. J. Int. Neural Netw. Soc.* **2016**, *73*, 70. [CrossRef] [PubMed]
12. Jacklin, S.A.; Haber, A.; de Simone, G.; Norman, T.R.; Kitaplioglu, C.; Shinoda, P. *Full-Scale Wind Tunnel Test of an Individual Blade Control System for a UH-60 Helicopter*; National Aeronautics And Space Administration Moffett Field Ca Ames Research Center: Mountain View, CA, USA, 2002.
13. Glickman, S.; Kulessky, R. Identification-based PID Control Tuning for Power Station Processes. *IEEE Trans. Control. Syst. Technol.* **2004**, *12*, 123–132. [CrossRef]
14. Furst, D.; Auspitzer, T. Numerical Investigation of Vibration Reduction through IBC for a 20to Helicopter Rotor Model. In Proceedings of the 28th European Rotorcraft Forum, Bristol, UK, 17–20 September 2002.
15. Wang, C.; Lu, Y.; Chen, R. Effect of Active Blade Pitch Control on Helicopter Rotor Performance. *J. Aerosp. Power* **2014**, *29*, 1922–1929.
16. Jian, W.; Wang, H. Development of Swash Plate-less Helicopter Blade Pitch Control System Using the Limited Angle Direct-drive Motor (LADDM). *Chin. J. Aeronaut.* **2015**, *6028*, 1416–1425.
17. Xu, H. Research on Rotor Control and Vibration Reduction Based on Individual Blade Control. Master's Thesis, Nanjing University of Aeronautics & Astronautics, Nanjing, China, 2016.
18. Yang, R. Calculation and Analysis of Rotor Vibration Load Based on Individual Blade Control. Master's Thesis, Nanjing University of Aeronautics & Astronautics, Nanjing, China, 2017.
19. Gu, J. Research on Adaptive Individual Blade Control of Helicopter Vibration. Master's Thesis, Nanjing University of Aeronautics & Astronautics, Nanjing, China, 2018.
20. Gu, J.; Li, Q.; Gao, Y. Analysis on Rotor Vibration Load in Individual Blade Pitch Control. *J. Nanjing Univ. Aeronaut. Astronaut.* **2018**, *4*, 155–161. [CrossRef]
21. Bir, G. *University of Maryland Advanced Rotorcraft Code (UMARC) Theory Manual*; University of Maryland: College Park, MD, USA, 1994.
22. Leishman, J.G.; Beddoes, T.S. A Semi-Empirical Model for Dynamic Stall. *J. Am. Helicopter Soc.* **1989**, *34*, 3–17.
23. Dan, P.; Liu, L.; Chandrasekar, J.; Bernstein, D.S.; Friedmann, P.P. Higher-Harmonic-Control Algorithm for Helicopter Vibration Reduction Revisited. *J. Guid. Control. Dyn.* **2012**, *28*, 918–930.
24. Shi, Y.; Zhao, Q.; Xu, G. Numerical Calculation and Parametric Study of Aerodynamics of Rotor Blade-vortex Interaction. *Hangkong Xuebao* **2010**, *31*, 1106–1114.4. [CrossRef]
25. Shi, Y.; Xu, G. Research on the Influence of Flight Parameters on Helicopter Rotor BVI Noise Characteristics. *Hangkong Xuebao* **2013**, *34*, 2520–2528.
26. Wang, L.; Xu, G.; Shi, Y. Influence of Higher Harmonic Control on Airload and Acoustics of Rotor Blade-vortex Interaction. *Hangkong Xuebao* **2017**, *38*, 65–74. [CrossRef]
27. Feng, J.; Lu, Y.; Xu, J. Research on the Effect of Open-loop Active Blade-pitch Control on Rotor BVI Noise Alleviation. *Hangkong Xuebao* **2014**, *35*, 2901–2909. [CrossRef]
28. Chen, S.; Zhao, Q.; Ni, T. Rotor Noise Reduction Mechanism and Parameter Analysis of HHC Method. *Hangkong Xuebao* **2017**, *38*, 11–24. [CrossRef]
29. Ni, T.; Zhao, Q.; Ma, S. Active Control Mechanism of Rotor BVI Noise Based on IBC Method. *Hangkong Xuebao* **2017**, *38*, 120–132. [CrossRef]

30. Wei, R.; Lu, Y.; Dong, X.; Feng, J. Noise Active Control of Electrically Controlled Rotor in Hover. *J. Nanjing Univ. Aeronaut. Astronaut.* **2018**, *50*, 96–101. [CrossRef]
31. Fogarty, D.E.; Wilbur, M.L.; Sekul, M.K. A Computational Study of BVI Noise Reduction Using Active Twist Control. In Proceedings of the American Helicopter Society 66th Annual Forum, Phoenix, AZ, USA, 11–13 May 2010.
32. Anobile, A.; Bernardini, G.; Gennareti, M. Active twist rotor controller identification for blade vortex interaction noise alleviation. In Proceedings of the 19th AIAA/CEAS Aeroacoustics Conference, Berlin, Germany, 27–29 May 2013.
33. Padthe, A.K.; Friedmann, P.P. Simultaneous BVI Noise and Vibration Reduction in Rotorcraft Using Microflaps including the Effect of Actuator Saturation. In Proceedings of the American Helicopter Society 68th Annual Forum, Fort Worth, TX, USA, 1–3 May 2012.